

Supplementary Material: Thermal impact of magmatism in subduction zones

David W. Rees Jones*, Richard F. Katz, Meng Tian

Department of Earth Sciences, University of Oxford, South Parks Road, Oxford, OX1 3AN, UK.

John F. Rudge

Department of Earth Sciences, Bullard Laboratories, University of Cambridge, Madingley Road, Cambridge CB3 0EZ, UK.

Abstract

The Supplementary Material contains further details of the petrological model of melting (Sec. S1), the 1D column model (Sec. S2), and the 2D thermal model (Sec. S3).

S1. Petrological model of hydrous flux melting

In the 1D column model, we use a simple petrological model of hydrous flux melting, which is the dominant form of melting in subduction zones. The model was inspired by previous studies [1, 2, 3], and is developed as follows. First, we restrict attention to a ternary system. The three components should not be thought of as identifiable minerals or oxides but rather as idealized components chosen to capture the physics in which we are interested. We start with two components that can be considered ‘refractory’ and ‘fertile’ [4, 5]. To this system, we add a third component to represent volatiles. We initially take this component to be ‘water’ and we consider that the concentration of ‘water’ is relatively small. One role of this third hydrous component is to depress the solidus temperature.

*Corresponding author

Email address: `David.ReesJones@earth.ox.ac.uk` (David W. Rees Jones)

Our second simplification is to use a quasi-linear phase diagram. This can be thought of as a linearization of the ternary phase loops used by Ref. [3] about some initial composition.

Our third simplification is that the melting/solidification reactions happen sufficiently rapidly that a partially molten region is at local thermodynamic equilibrium. This implies that compositions of the coexisting solid and liquid phases are given exactly by the phase diagram.

S1.1. Mathematical description of phase diagram

The solidus temperature increases with increasing pressure at a rate γ . We linearize the dependence of the solidus on chemical composition. Since the sum of the concentrations of the components is unity, we need only specify two linear coefficients M_2, M_3 for the fertile and water components respectively, both of which lower the solidus temperature. Thus the solidus temperature

$$T_s = T_{s0} - \rho g z / \gamma - M_2 c_2^s - M_3 c_3^s. \quad (\text{S5})$$

This expression can be rearranged to give, for example, the solidus concentration c_2^s as a function of temperature, depth, and concentration of the third component. An interpretation of equation (S5) can be made by identifying $T_{s0} - \rho g z / \gamma$ with the solidus temperature of the refractory component at given depth z , which in this section is negative.

We assume that the liquidus concentration is related to the solidus concentration as follows:

$$c_2^l = c_2^s + \Delta c_2, \quad (\text{S6})$$

$$c_3^l = c_3^s + \Delta c_3. \quad (\text{S7})$$

For the simplest case we take $\Delta c_{2,3}$ to be constants, but we will also consider generalizations.

S1.2. Choice of parameter values and implications for melting

We choose parameters in our model to constrain the degree of so-called ‘batch melting’ as a function of temperature and pressure:

$$F = \frac{\widetilde{c}_{0j} - c_j^s}{c_j^l - c_j^s}. \quad (\text{S8})$$

Batch melting refers to the degree of melting experienced by a sample raised to given temperature and pressure conditions assuming no extraction of melt. The composition \widetilde{c}_{0j} is the composition of the solid mantle before the onset of melting. We then combine equations (S5)–(S7), which apply for each j , with equation (S8) to obtain

$$F = \frac{\widetilde{c}_{03} - c_3^s}{\Delta c_3} = \frac{T - T_{s0} + \rho g z / \gamma + M_2 \widetilde{c}_{02} + M_3 \widetilde{c}_{03}}{M_2 \Delta c_2 + M_3 \Delta c_3}. \quad (\text{S9})$$

A key quantity is the isobaric productivity $\partial F / \partial T$. If Δc_2 and Δc_3 are constants, then the isobaric productivity is a constant

$$\frac{\partial F}{\partial T} = \frac{1}{M_2 \Delta c_2 + M_3 \Delta c_3}. \quad (\text{S10})$$

Thus melt is produced at a constant rate with increasing temperature. Linear models of two component melting already include this effect [e.g. 5]. It is worth noting that the productivity is reduced by the third, hydrous component.

In this formulation, volatiles do indeed depress the solidus temperature. However, in addition to depressing the solidus, volatiles are also associated with a ‘low-productivity tail’ [1]. The initial melting above the solidus temperature is less productive than later melting:

$$\left. \frac{\partial F}{\partial T} \right|_{F=0} < \left. \frac{\partial F}{\partial T} \right|_{F=1}. \quad (\text{S11})$$

The purely linear model does not satisfy this constraint, because the productivity is constant. Therefore, we generalize our model to allow for a low-productivity tail. Volatiles are incompatible and partition into the melt with a partitioning coefficient D defined by

$$c_3^s = D c_3^l \Rightarrow \Delta c_3 = c_3^s (1/D - 1), \quad (\text{S12})$$

where $D \ll 1$ for incompatible, volatile elements. We assume that D is constant. However, Δc_3 is no longer constant, instead depending on composition, and hence pressure and temperature. Upon a little rearrangement, we find

$$\begin{aligned} T - (T_{s0} - \rho g z / \gamma - M_2 \widetilde{c}_{02} - M_3 \widetilde{c}_{03}) \\ = (M_2 \Delta c_2 / \Delta c_3 + M_3)(\widetilde{c}_{03} - c_3^s), \end{aligned} \quad (\text{S13})$$

which can be rearranged to give a quadratic equation for c_3^s , recalling that Δc_3 is proportional to c_3^s . The degree of melting F is no longer a linear function (however it can be computed explicitly using the quadratic formula so there is no computational difficulty, unlike more complex nonlinearities where iterative methods are required to solve for F). We can calculate the isobaric productivity at $F = 0$ and $F = 1$ and find

$$\left. \frac{\partial F}{\partial T} \right|_{F=0} = [M_3 \widetilde{c}_{03}(1/D - 1) + M_2 \Delta c_2]^{-1}, \quad (\text{S14})$$

$$\left. \frac{\partial F}{\partial T} \right|_{F=1} = [M_3 \widetilde{c}_{03} D(1 - D) + M_2 \Delta c_2]^{-1}. \quad (\text{S15})$$

We can interpret the effective isobaric productivity of the mixture as the harmonic mean of productivities associated with the fertile and volatile component. Typically, the contribution of the volatile component dominates at small F and the fertile component dominates at large F because

$$M_3 \widetilde{c}_{03} D(1 - D) \ll M_2 \Delta c_2 \ll M_3 \widetilde{c}_{03}(1/D - 1). \quad (\text{S16})$$

Our formulation thus achieves the low-productivity tail expected physically; and it recovers the fertile–refractory system in the absence of volatiles.

To summarize, the degree of melting increases over the temperature range

$$T(F = 0) = T_{s0} - \rho g z / \gamma - M_2 \widetilde{c}_{02} - M_3 \widetilde{c}_{03}, \quad (\text{S17})$$

$$T(F = 1) = T_{s0} - \rho g z / \gamma - M_2 \widetilde{c}_{02} + M_2 \Delta c_2 - M_3 D \widetilde{c}_{03}. \quad (\text{S18})$$

The gradient of the function $F(T)$ at these endpoints is given by equations (S14) and (S15).

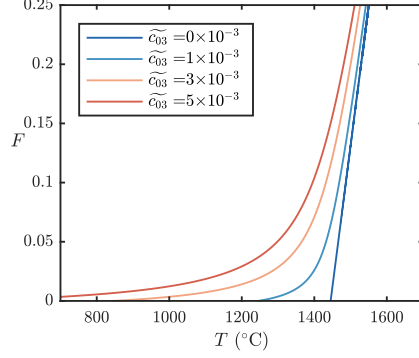


Figure S1: The degree of melting F as a function of temperature T at increasing water concentration \widetilde{c}_{03} . Other parameters were fixed, namely $T_{s0} - \rho g z / \gamma = 1550$ °C at $z = 100$ km, $M_2 = 700$ °C, $M_3 = 2 \times 10^5$ °C, $D = 0.01$, $\Delta c_2 = 0.6$, and $\widetilde{c}_{02} = 0.15$. These parameter values are motivated by Ref. [2].

Thus a limited number of parameters can describe a significant range of realistic melting behaviours, as shown in Fig. S1. For the anhydrous, fertile–refractory part of the system, we use $T_{s0} = 1100$ °C, $\rho g / \gamma = 4.5 \times 10^{-3}$ °C/m, $M_2 = 700$ °C, $\Delta c_2 = 0.6$, and $\widetilde{c}_{02} = 0.15$. This ensures that we match the anhydrous melting curve of Ref. [2], particularly around 3 GPa. For the hydrous part of the system, we use $M_3 = 2 \times 10^5$ °C, $D = 0.01$. These parameter values were chosen to roughly match the hydrous melting curve of Ref. [2], particularly around 3 GPa with 0.5 wt% water. Although the precise parameter values are in the right region for consistency with previous studies and their associated experimental libraries, as well as inferences from field observations, this parameterization is too simple to reproduce all the features observed experimentally. However, it can reproduce the two main features: solidus depression and a low-productivity tail.

S1.3. Generalized model: accounting for saturation in water

The addition of more water does not indefinitely lower the solidus, because eventually water becomes saturated in the liquid phase. The amount of water

that dissolves increases with pressure; Ref. [2] uses the formula

$$X_{\text{H}_2\text{O}}^{\text{sat}} = 12.00P^{0.6} + 1.00P, \quad (\text{S19})$$

where the pressure P is measured in GPa. This is well constrained by experiment below 2 GPa, and constrained indirectly at higher pressures. This corresponds to a critical degree of melting and critical temperature below which the degree of melting drops rapidly to zero, as shown in Fig. S2c, for example.

Our modelling approach is to mimic this behaviour by modifying the phase diagram. We first compute the corresponding critical solid saturation point c_{sat}^s , using equation (S19) for the liquid saturation and the partition coefficient of equation (S12). For temperatures below this point, we change the freezing point depression coefficient:

$$T_s = T_{s0} - \rho g z / \gamma - M_2 c_2^s - M_4 (c_3^s - c_{\text{sat}}^s) - M_3 c_{\text{sat}}^s, \quad (\text{S20})$$

where $M_4 \leq M_3$. Note that the previous model is a special case $M_4 = M_3$, and a eutectic-like phase diagram can be obtained by the special case $M_4 = 0$. In practice, we find $M_4 = M_3/50$ makes a decent approximation to Ref. [2], as shown in Fig. S2. This means that the initial productivity near $F = 0$ is a factor $M_3/M_4 = 50$ times greater. We use this generalized model to assess the significance of the increased productivity near water saturation in Fig. 3 of the main text.

S2. Further details of one-dimensional column model

In the context of a one-dimensional melting model, mass conservation imposes a strong constraint on the model behaviour in steady state. We adopt an extended Boussinesq approximation in which density differences between the phases are neglected except for their role in driving buoyant liquid segregation. There are several equivalent ways to present the following equations; we approach the problem by considering conservation in the liquid phase and in the two-phase composite.

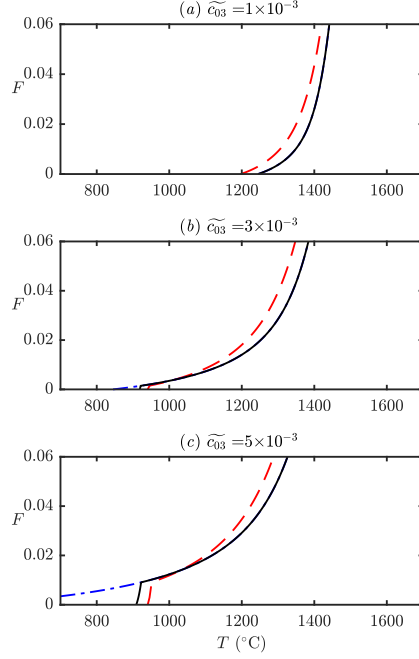


Figure S2: The degree of melting $F(T)$ produced by our revised model (solid black) and the parameterization of Ref. [2] (dashed red). Results computed at fixed pressure (3 GPa, corresponding to $z = 100$ km) at increasing water content: (a) $\widetilde{c}_{03} = 1 \times 10^{-3}$, (b) $\widetilde{c}_{03} = 3 \times 10^{-3}$, and (c) $\widetilde{c}_{03} = 5 \times 10^{-3}$. Note the kink in the curves around 950°C in (b, c), which is associated with water saturation. Without this saturation behaviour, our standard model predicts melting at several hundred degrees cooler temperatures (dashed blue curves).

Mass conservation gives

$$\frac{d}{dz}(\phi w^l) = \frac{\Gamma}{\rho}, \quad (\text{S21})$$

$$\frac{d}{dz}\bar{w} = 0, \quad (\text{S22})$$

where $\bar{x} = x^s(1 - \phi) + x^l\phi$ denotes an average over the solid and liquid phases, with volume fractions $(1 - \phi)$ and ϕ respectively. The vertical velocity is w , volumetric melting rate is Γ and density is ρ . We first integrate equation (S22) to obtain

$$\frac{\phi w^l}{W_0} + \frac{(1 - \phi)w^s}{W_0} = 1, \quad (\text{S23})$$

where \overline{W}_0 is the total volume flux at the bottom of the melting column (which is not the motion of the solid phase alone, unlike in upwelling mantle columns used in the context of mid-ocean ridge magmatism). We follow the approach of Ref. [4] and define the quantity $F = \phi w^l / \overline{W}_0$. Thus the scaled, liquid-phase volume flux is F and the scaled solid phase volume flux is $(1 - F)$.

We can recover our previous definition of F in equation (S8) by considering conservation of species mass. For each component $j = 1, 2, 3$,

$$\frac{d}{dz}(\phi w^l c_j^l) = \frac{\Gamma_j}{\rho}, \quad (\text{S24})$$

$$\frac{d}{dz} \overline{w c_j} = 0. \quad (\text{S25})$$

Note that, by summing equation (S24) over j and comparing with equation (S21), $\sum_j \Gamma_j = \Gamma$. We integrate equation (S25) and use equation (S23) to obtain

$$F c_j^l + (1 - F) c_j^s = \frac{\overline{W}_0 c_{0j}}{\overline{W}_0} \equiv \widetilde{c}_{0j}. \quad (\text{S26})$$

We then determine the degree of melting F , which is controlled by an energy equation and our phase diagram. One unusual feature of subduction zones is the non-monotonic temperature profile, which is largely controlled by the flow of the solid mantle. As described in the main text, we use a steady energy balance for a one-dimensional column

$$\rho c_p \overline{W}_0 \frac{dT}{dz} = -L\Gamma + \frac{d}{dz} \left(\rho c_p \kappa \frac{dT}{dz} \right) + \rho c_p \Psi, \quad (\text{S27})$$

with a volumetric source term $\rho c_p \Psi$ that represents the heat supplied by large-scale mantle corner flow. In the absence of melting, the final pair of terms on the right-hand side establishes a non-monotonic temperature profile. Note that we do not solve momentum equations because only the two-phase average velocity \overline{W}_0 , which is constant as a result of mass conservation, appears in the heat equation (S27).

Next we observe that $\overline{W}_0 F' = \Gamma / \rho$ and F' is proportional to the isobaric productivity discussed previously, namely $F' = (T' + \rho g / \gamma) \partial F / \partial T$. We can better understand the system by rescaling the energy equation. We scale lengths

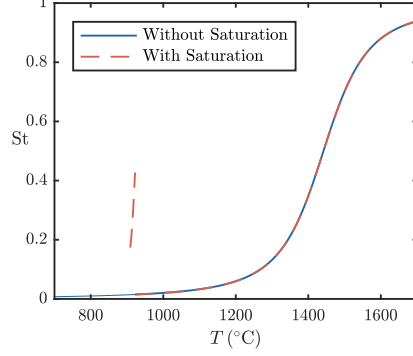


Figure S3: Stefan number $St = (L/c_p)\partial F/\partial T$ at $P = 3$ GPa with and without modified phase diagram to account for water saturation, as discussed in section S1.3. Note that there is now an interval of higher isobaric productivity between the solidus temperature and the temperature at which the melt ceases to be saturated.

by H (the depth of the melting column), and the source term by κ/H^2 . The dimensionless parameters involved are a Péclet number $Pe = H\overline{W}_0/\kappa$, a Stefan number $St = (L/c_p)\partial F/\partial T$, a temperature change $\Delta T_H = \rho g H/\gamma$. Then the energy equation is

$$T'' = -\Psi + Pe [T'(1 + St) + St \Delta T_H], \quad (0 \leq z \leq 1). \quad (\text{S28})$$

A scaled version of the melting rate is

$$\tilde{\Gamma} \equiv \frac{H^2}{\kappa} \frac{\Gamma}{\rho} = Pe \frac{\partial F}{\partial T}(T' + \Delta T_H), \quad (\text{S29})$$

which has units of degrees Kelvin. Equation (S28) is subject to boundary conditions on T at $z = 0$ and $z = 1$. In general, the Péclet number is fixed but the Stefan number depends on temperature and pressure (hence depth), as well as the compositional parameters of our melting model. We plot the Stefan number in Fig. S3.

Our column-model approach is as follows. Extract a vertical temperature profile T_{ref} from a single-phase mantle flow and thermal model of a subduction zone, as shown in the main article. We then calculate $\Psi = -T''_{\text{ref}}(z)$. To investigate the effect of melting, we solve the rescaled energy equation, focussing on the

effect of varying the Péclet number and Stefan number (since the decompression term ΔT_H is well known). We present results in the main article.

S3. Further details of two-dimensional thermal model

Sources of fluids in subduction zones that trigger silicic magmatism are believed to be localized to particular depth ranges, associated with particular dehydration reactions in the subducting slab. Thus, in addition to the calculations presented in the main article, we also take three Gaussian magma flow profiles above the locations of the major dehydration reactions of the slab, with a position, magnitude and width suggested by Ref. [6]. We also consider the effect of all three sources combined.

As in the calculations in the main text, the principal result is that advective transport by magma substantially alters the thermal structure of subduction zones, as shown in Fig. S4. Flow associated with the peridotite source (*a*) is the most thermally significant, raising temperatures by over 200 K. Flow associated with the MORB source (*b*) raises temperatures near the trench by about 40 K; the gabbro source (*c*) is thermally insignificant. The peridotite source is strongest because it is associated with the largest magma flux. The MORB source is weaker because the flux is smaller and also because it occurs nearer the trench than the peridotite source, which means that the mantle wedge above the MORB source is slightly cooler. The gabbro source is especially weak because the flux is smaller, and because it is narrower than the other sources, and so tends to diffuse laterally more strongly. The combined set of sources (*d*) is dominated by the peridotite source, although there are also slightly elevated temperatures in the fore-arc region associated with the MORB source.

References

- [1] M. M. Hirschmann, P. D. Asimow, M. S. Ghiorso, E. M. Stolper, Calculation of peridotite partial melting from thermodynamic models of minerals and melts. III. Controls on isobaric melt production and the ef-

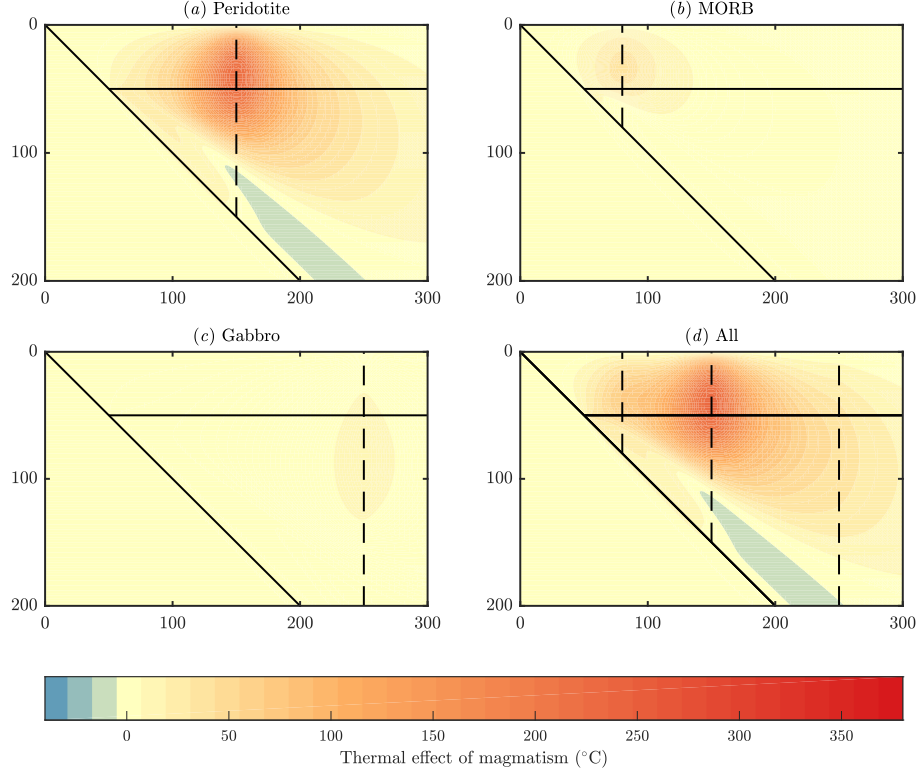


Figure S4: The thermal impact of magmatism ($T - T_{\text{ref.}}$) associated with the dehydration of (a) peridotite, (b) MORB, and (c) gabbros. We also show (d) results when all three sources are combined. We indicate the individual sources as dashed lines at the centre of each Gaussian pulse. Horizontal and vertical scales are distance from the trench (units km).

fect of water on melt production, J. Petrol. 40 (5) (1999) 831–851.
doi:10.1093/petroj/40.5.831.

[2] R. F. Katz, M. Spiegelman, C. H. Langmuir, A new parameterization of hydrous mantle melting, Geochem. Geophys. Geosyst. 4 (9).
doi:10.1029/2002GC000433.

[3] T. Keller, R. F. Katz, The role of volatiles in reactive melt transport in the asthenosphere, J. Petrol. 57 (6) (2016) 1073–1108.
doi:10.1093/petrology/egw030.

- [4] N. M. Ribe, The generation and composition of partial melts in the Earth's mantle, *Earth Planet. Sci. Lett.* 73 (2) (1985) 361–376. doi:10.1016/0012-821X(85)90084-6.
- [5] I. J. Hewitt, Modelling melting rates in upwelling mantle, *Earth Planet. Sci. Lett.* 300 (3–4) (2010) 264 – 274. doi:10.1016/j.epsl.2010.10.010.
- [6] C. R. Wilson, M. Spiegelman, P. E. van Keken, B. R. Hacker, Fluid flow in subduction zones: The role of solid rheology and compaction pressure, *Earth Planet. Sci. Lett.* 401 (2014) 261 – 274. doi:10.1016/j.epsl.2014.05.052.